PNAS RESEARCH ARTICLE | BIOPHYSICS AND COMPUTATIONAL BIOLOGY

Mechanism of voltage gating in the voltage-sensing phosphatase Ci-VSP

Rong Shen[a,1], Yilin Meng[a], Benoît Roux[a], and Eduardo Perozo[a,1]

Edited by William Catterall, University of Washington, Seattle, WA; received April 18, 2022; accepted August 24, 2022

Conformational changes in voltage-sensing domains (VSDs) are driven by the transmembrane electric field acting on the protein charges. Yet, the overall energetics and detailed mechanism of this process are not fully understood. Here, we determined free energy and displacement charge landscapes as well as the major conformations visited during a complete functional gating cycle in the isolated VSD of the phosphatase Ci-VSP (Ci-VSD) comprising four transmembrane helices (segments S1 to S4). Molecular dynamics simulations highlight the extent of S4 movements. In addition to the crystallographically determined activated "Up" and resting "Down" states, the simulations predict two Ci-VSD conformations: a deeper resting state ("down-minus") and an extended activated ("up-plus") state. These additional conformations were experimentally probed via systematic cysteine mutagenesis with metal-ion bridges and the engineering of proton conducting mutants at hyperpolarizing voltages. The present results show that these four states are visited sequentially in a stepwise manner during voltage activation, each step translocating one arginine or the equivalent of ~1 e_0 across the membrane electric field, yielding a transfer of ~3 e_0 charges in total for the complete process.

voltage dependence | gating currents | energy landscape | Ci-VSP

Significance

The voltage-sensing phosphatase Ci-VSP serves as an electrochemical signaling center. Membrane potential modulates a PTEN-like phosphatase activity, leading to dephosphorylation of phosphoinositides and the downstream regulation of ion channels and transporters. The structures of Ci-VSP voltage sensor domain (Ci-VSD) offer the opportunity to carry out a detailed analysis of the energetics of gating charges and S4 reorientations under an electric field. The combined computational and electrophysiological approach to these questions revealed two additional VSD conformations and shows that voltage activation involves sequentially populating four S4 conformations in a stepwise process, fulfilling a general "click" model of VSD rearrangement.

Voltage-sensing domains (VSDs) are conserved functional modules that transduce voltage-driven charge rearrangements to exert conformational biases on effector domains present in a variety of membrane proteins (1–4), including ion channels, solute carriers, and phosphatases. They form an antiparallel bundle of four transmembrane helices referred to as segments S1 to S4. A series of positively charged high-pK_a (negative logarithm of association constant) residues (mostly arginines) located along the S4 segment act as the key structural element for voltage sensing (5–8), referred to as "gating" charges because their movements is associated with the opening of the activation gate of ion channels. The S4 gating charge motif varies in different VSDs (9–14), a fact that leads to a diversity of voltage-sensing profiles. These positive charges make extensive and sequential salt-bridge interactions with negative countercharges on segments S1 to S3 (and lipid headgroups) upon S4 translocation (15–19). At the center of VSDs, a single layer of in-plane hydrophobic residues on the S1 to S3 segments, alternatively referred to as the hydrophobic plug, the charge-transfer center, or the hydrophobic gasket (20–23), serves to electrically separate the intra- and extracellular aqueous vestibules of the VSD, leading to a dramatic focusing of the electric field over a distance much shorter than the total membrane thickness (24, 25).

In addition to mediating ion and/or proton conduction across the membrane, VSDs are able to precisely control enzyme activity in voltage-sensing phosphatases. Ci-VSP was the first member of the VSP family that showed robust membrane potential dependent enzymatic activity toward inositol phospholipids, a crucial second messenger that plays a key role in a myriad of basic cellular functions (4, 26). Ci-VSP has an N-terminal transmembrane VSD and a C-terminal cytosolic phosphatase domain, homologous with the tumor suppressor phosphatase PTEN (protein lipid phosphatase and tensin homolog deleted on chromosome 10), but with a broader substrate specificity than PTEN (27–31). Ci-VSP is likely a monomer in the native membrane environment and functions independently even at high expression level (32, 33). Furthermore, a single mutation at the catalytic center of the phosphatase domain of Ci-VSP can eliminate its enzymatic activity with little effect on electrical sensitivity of the VSD (4), making Ci-VSP an ideal model for studying the gating mechanism of the VSD itself.

To date, there is no atomic structure of any full-length VSPs available; however, crystal structures of Ci-VSD have been determined in two different states ("Up" and "Down"; *SI Appendix*, Fig. S1*A*), providing an initial atomistic view of the voltage-driven conformational change within a given VSD (20). A recent set of cryo-electron microscopy (cryo-EM) structures of voltage-dependent ion channels has shown that these initial results highlight key mechanistic commonalities among VSD-driven

Author affiliations: [a]Department of Biochemistry and Molecular Biology, The University of Chicago, Chicago, IL 60637

Author contributions: R.S., B.R., and E.P. designed research; R.S. and Y.M. performed research; Y.M. contributed new reagents/analytic tools; R.S., B.R., and E.P. analyzed data; and R.S., B.R., and E.P. wrote the paper.

The authors declare no competing interest.

This article is a PNAS Direct Submission.

[1]To whom correspondence may be addressed. Email: shenr@uchicago.edu or eperozo@uchicago.edu.

This article contains supporting information online at http://www.pnas.org/lookup/suppl/doi:10.1073/pnas.2206649119/-/DCSupplemental.

Published October 24, 2022.

systems (34–37). From the two Ci-VSD structures, the elementary S4 movement is best characterized by a helix turn and axial translocation (three-residue, or one "click") movement, while S1 to S3 display little or no conformational change. This movement is broadly consistent with the classic helical screw model, whereby the S4 helix translates along and rotates around its main axis (38, 39), resulting in the translocation of one arginine residue across a region near the center of the VSD where the transmembrane electric field is focused to yield an estimated gating charge of ~1 e_0 (20). Due to the inherent difficulty, no experimental result of the total amount of gating charges of Ci-VSP has been reported yet. However, voltage clamp fluorometry and enzyme activity assays show that Ci-VSP has distinct substrate preferences at different depolarization membrane potentials, pointing to the likelihood of multiple Ci-VSD stable states undergoing multistep conformational transitions during a complete functional sequence (28, 31, 32). Here, we evaluate the full conformational space of a VSD as a function of voltage and displacement by combining 1) the computation of free energy and displacement charge landscapes in Ci-VSD, 2) estimating the number of energetically stable conformations, and 3) experimentally evaluating them by means of metal-ion bridges and the engineering of proton-conducting mutants. This interrelated approach offers the most detailed insight to date on the mechanism of electric field transduction in VSDs.

Results

Free Energy Landscapes and Major Functional States Governing Ci-VSD Gating Cycle. Inspired by the charge–countercharge "click" model proposed from the structural study of Ci-VSD (20), we evaluated the existence of extended S4 movements beyond those observed experimentally. This hypothesis is based on the assumption that additional charge–countercharge partnerships are possible with additional S4 movements and limited changes in the S1 to S3 countercharges. Any additional S4 movements beyond the experimentally determined Up and Down conformations might lead to the identification of novel, energetically favorable charge–countercharge interactions. To this end, we generated two homology models of Ci-VSD in the "up-plus" (one "click" beyond Up) and "down-minus" (one "click" below Down) states and equilibrated them using molecular dynamics (MD) simulations (*SI Appendix*, Fig. S1 *A–C*). To characterize the stability of these states and inform the details of the gating mechanism, we calculated the free energy landscapes governing the conformational transition process and the related displacement charges, $Q_d = \langle \sum_i q_i z_i / L_z \rangle$, representing the energetic coupling between the transmembrane potential and the VSD (Fig. 1 *A* and *B*). Observable gating charges are determined from the difference in Q_d between two conformations. Two-dimensional potentials of mean force (PMFs) at three membrane potentials (0 and ±150 mV) were calculated using the Hamiltonian-replica exchange molecular dynamics (H-REMD) umbrella sampling simulations (*SI Appendix*, Fig. S1 *D–G*), with the translocation and rotation of S4 being used as reaction coordinates to describe the conformational change (*SI Appendix*, *Materials and Methods* for the detailed definition of these two collective valuables).

From these calculations the membrane potential biased the free energy landscape in the expected directions: A negative potential increased the population of the "down-minus" state, a positive potential increased the population of the "up-plus" state, and the "Down" and "Up"' states have the lowest free energies at 0 mV as anticipated from the crystallographic data. Interestingly, the "up-plus," "Up," and "Down" states were quite stable, populating at local free energy minima, at all three membrane potentials. Not so in the case of the "down-minus" state, which was found to be energetically unfavorable compared with the other three states, even if it stayed near its starting conformation during the initial MD simulation (Fig. 1*A* and *SI Appendix*, Fig. S1*C*). Distinctive free energy basins corresponding to intermediate metastable states have also been observed in the free energy landscapes (Fig. 1 *A* and *C*). Analysis of the trajectories showed that these metastable states represent an interval backbone movement of S4 compared with the adjacent main states. These movements take place while keeping the key salt-bridge interactions between the side chains of the gating residues on S4 and the countercharge residues on S1 to S3 or lipids mostly unchanged (Fig. 1*D*). This result suggests that the S4 backbone movement likely takes place ahead of the rearrangement of the side-chain salt-bridge interactions during gating. This is also in agreement with the displacement charge calculation result showing that the conformational change between two adjacent main states by moving an arginine across the electric filed focused at the center hydrophobic gasket contributes to an estimated gating charge of ~1 e_0 (Fig. 1 *B* and *C*). As a results, the complete functional cycle of the voltage sensor from the "down-minus" state to the "up-plus" state yields a total gating charge of ~3 e_0.

The S4 Segment of Ci-VSD Adopts an α-Helical Conformation during Gating. The secondary structure of S4 (α-helical and/or 3_{10}-helical) has attracted a lot of attention and debate, as it is directly related to the orientation and interacting network of the gating residues in different states, and thus the detailed VSD gating mechanism has converged toward two mechanistically related models: a "helical screw model," where the S4 has both rotational and translational movement, or a "helical sliding model," where the S4 translates along its principal axis with minimal rotational movements (34, 37). Both crystal structures and MD trajectories along the minimum free energy path of one of the free energy landscapes reveal that the Ci-VSD S4 segment tends to adopt a fully α-helical conformation during gating, with only one or two residues occasionally adopting a 3_{10}-helical conformation. This high α-helical propensity was not a result of the harmonic restraints applied in the PMF calculations, as the same trend was observed in the MD simulations without any restraint (Fig. 1 *E* and *F*). We suggested that it is the location of the countercharges (in other words the hydrogen-bonding network) that shapes the secondary structure of S4. To test this hypothesis, MD simulations were performed with an "up-plus" state model of Ci-VSD with double mutant D129S/A154E, in reference to the position of countercharges in the VSDs of potassium channels. During a 100-ns production MD run, the S4 segment adopted a perfect α-helical conformation. However, if two hydrogen-bonding interactions between the gating residues and countercharges (R223−D136 and R226−A154E) were enforced at the very beginning of the simulation, the extracellular region of S4 spontaneously changed into a 3_{10}-helix in the following simulation without any restraints. This α-helix to 3_{10}-helix transition placed the four arginine residues all toward the aqueous crevice of Ci-VSD and increased the hydrogen-bonding probability of the gating residues with the countercharges (*SI Appendix*, Fig. S2 *A–E*). In addition, the unfavorable hydrophobic environment will also modulate the orientation of the gating residues, which in turn regulates the secondary conformation of the S4 segment (37). Using the KAT1 potassium channel as an example (13), if the

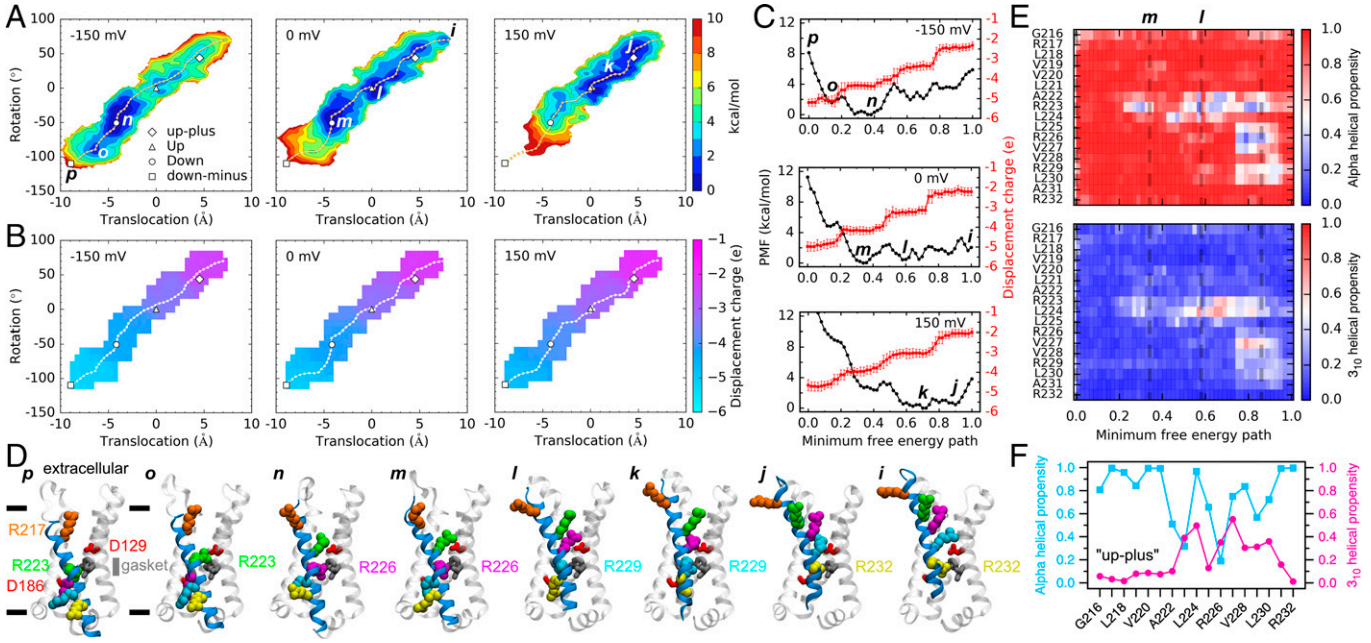

Fig. 1. Free energy landscapes, gating charges, and conformational changes in the movement of the VSD S4 segment at different membrane potentials. (*A*) Two-dimensional PMFs of the gating process at −150 mV, 0 mV, and 150 mV. Translocation and rotation of the S4 segment along and around its principal axis are used as the reaction coordinates, respectively. The dashed lines represent the minimum free energy paths (MFEPs). Projection of the four starting configurations onto the two reaction coordinates and representative local minima along the MFEPs are highlighted. (*B*) Average displacement charge, $Q_d = \langle \sum_i q_i z_i / L_z \rangle$, at different membrane potentials. Snapshots (n = 50) from the last 5-ns trajectories of the H-REMD simulations were used for the calculation. The dashed lines are the MFEPs as in *A*. (*C*) One-dimensional PMF and the average displacement charge along the MFEP at different membrane potentials. Error bars denote SD. (*D*) Snapshots of the representative local minima. The positive charged residues on the S4 segment are shown in the van der Waals (vdW) representation with different colors. The two countercharges D129 (S1) and D186 (S3) and the hydrophobic gasket forming residues I126 (S1), F161 (S2), and I190 (S3) are displayed as sticks. The gray and black bars represent the approximate position of the hydrophobic gasket and membrane bilayer, respectively. (*E*) Propensity of S4 residues adopting an alpha helical (*Top*) or a 3_{10} helical (*Bottom*) conformation along the MFEP of the H-REMD simulation at 0 mV. Residue i is classified to adopt an alpha helical or a 3_{10} helical conformation when it forms a hydrogen bond ($d_{O\text{-}N}$ < 3.5 Å and $\alpha_{O\text{-}H\text{-}N}$ > 120°) to residue $i + 4$ or $i + 3$, respectively. The VSD structures from the last 5 ns trajectory were used for the calculation (n = 100). The vertical dashed lines represent the approximate locations of the four major states along the MFEP. (*F*) The α-helical and 3_{10} helical propensities for S4 residues of the "up-plus" state VSD during the MD simulation without any restraint. The VSD structures from the last 10-ns trajectory were used for the calculation (n = 1,000).

central region of S4 does not adopt a 3_{10}-helical conformation, the arginine residues on the extracellular side will face the hydrophobic VSD-pore domain interface or the hydrophobic lipid tails, which is highly energetically unfavorable (*SI Appendix*, Fig. S2 *F–I*).

State-Dependent Residue–Residue Interactions Probed by Cd^{2+} Bridges. Efforts to obtain structural correlates of the two predicted states, "up-plus"' and "down-minus," have been frustrated by the size, biochemical stability, and/or crystallization hurdles. However, we have carried out a metal bridge experimental strategy to evaluate the extended conformational landscape in Ci-VSD, characterize all predicted conformations, and explore the existence of other putative states. To this end, we introduced cysteine mutations in the VSD, guided by our computational models, and evaluated the formation of Cd^{2+} bridges to identify the dynamic residue–residue interactions during the functional cycle (17, 21). Combined with restrained MD simulations with an explicit Cys–Cd^{2+}–Cys bridge (40, 41), we then established the most likely state at which each specific interaction can be formed.

We studied the Cd^{2+} effect on the net OFF gating charge (Q) of single cysteine mutants using the cut-open oocyte voltage clamp technique (*SI Appendix*, Fig. S3). For wild-type (WT) Ci-VSP, single S1 (M133C, L137C), S2 (A154C), and S3 (T197C) and the intracellular side of S4 (L224C–R232C) mutants, 100 μM Cd^{2+} has little effect on the normalized Q at the maximum depolarization potential (Fig. 2*A*). However, the Q–V curve of A154C shifted toward more positive voltages compared to others. This effect can be restored after washing with the metal chelator dithiothreitol or EGTA (Fig. 2*B*). In contrast, A154E showed little response to the external Cd^{2+} over the whole range of the voltage pulses. We interpreted this result to suggest that Cd^{2+} could get into the external crevice and bind at the site near A154C, slowing the movement of S4 at lower voltages as shown in the gating current traces (*SI Appendix*, Fig. S3 *A* and *B*). As a result, we used the A154E mutant instead of A154C in the following double-mutant experiments to reduce the Cd^{2+} effect from single mutants. It is worth noting that the mutant R223C enabled a continuous proton current through the VSD at negative potentials, consistent with observations in the mutant R223H (42) and analogous mutants of ion channels (43, 44). Thus, changes in steady-state currents were used in the study of the Cd^{2+} effect on R223C (*SI Appendix*, Fig. S3*C*). Surprisingly, an apparent decrease of the maximum charge was observed for Y200C. As there are plenty of negative residues at the extracellular face of the VSD, potential formation of Cd^{2+} bridges between the cysteine and glutamates/aspartates could be responsible for the net charge reduction (17). We found that neutralization of D136 (on S1) and each of the three negative residues on the S3–S4 loop (D204, E205, and E209) can lead to a partial relief of the Cd^{2+} effect, while a quadruple countercharge mutant (D136A/D204A/E205A/E209A) almost totally eliminated the Cd^{2+} effect and increased the kinetics of gating charge movement dramatically (*SI Appendix*, Fig. S4 *A–C*). MD simulations of Ci-VSD/Y200C showed that the Cd^{2+} binding at Y200C is located along the gating charge transfer pathway, so this bridge could impede the movement of the arginine residues

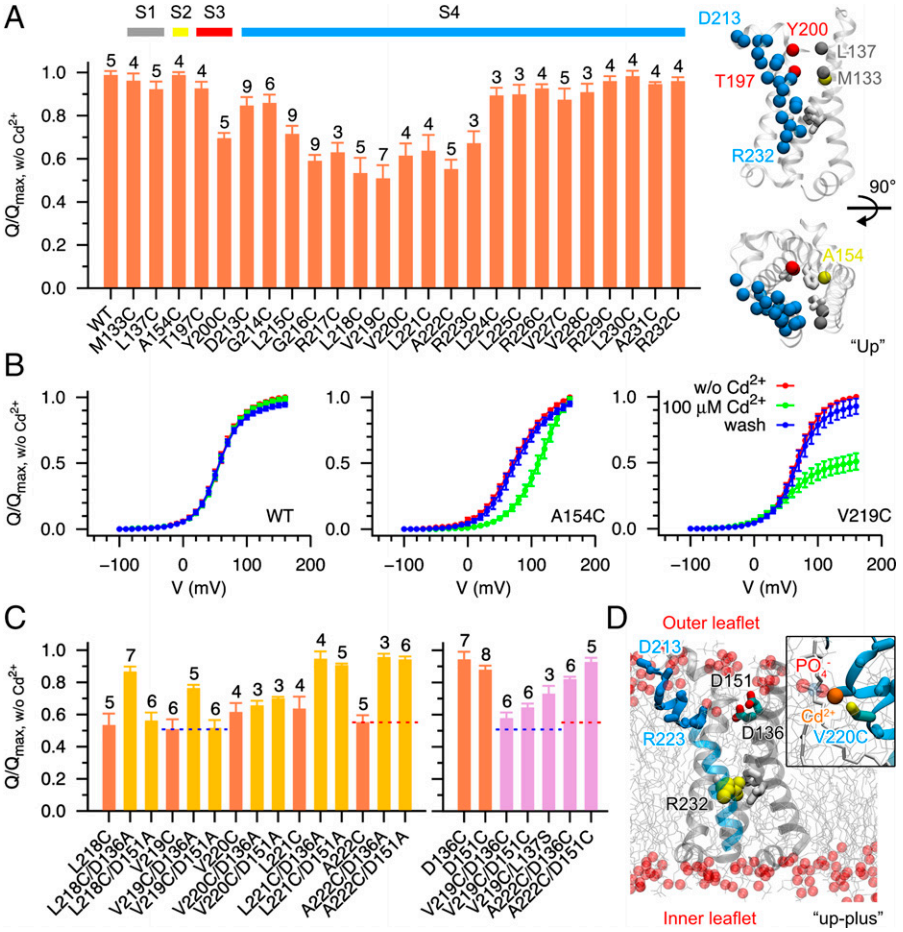

Fig. 2. Effect of extracellular cadmium (Cd^{2+}) ions on Ci-VSD charge movements from single cysteine mutations. (*A*, *Left*) The relative immobilization of OFF gating charge movement of WT and single cysteine mutants of Ci-VSP at the maximum voltage in response to 100 µM Cd^{2+}. The net charge *Q* is calculated by numerically integrating the OFF gating current, except for the R223C mutant that the maximum current at the end of the voltage pulse was used for the normalization and comparison. Error bars denote SD with the number of experiments being listed on the top of each of the bars. (*A*, *Right*) Side and top view of the "Up" state VSD (PDB ID code: 4G7V) with carbon alpha atoms of the mutants being highlighted in spheres with different colors: gray (on S1), yellow (on S2), red (on S3), and blue (on S4) and the hydrophobic gasket forming residues in white sticks. (*B*) Representative charge-voltage (*Q-V*) curves in the absence (red), in the presence (green) and after washout (blue) of 100 µM Cd^{2+}. The *Q-V* curves were normalized with respect to the maximum net charge without (w/o) Cd^{2+} for each experiment. Error bars denote SD (WT, $n = 5$; A154C, $n = 4$; V219C, $n = 7$). (*C*) Countercharges D136 and D151 play indirect roles on external Cd^{2+} induced immobilization of OFF gating charge movement of single cysteine mutants on the extracellular side of S4 other than forming direct metal bridges. (*D*) A snapshot of the "up-plus" state VSD from MD simulations. Only parts of the lipid molecules (gray lines) and their nonester phosphate oxygen atoms (red spheres) are shown for clarity. The extracellular (residues: 213 to 223) and intracellular sides of the S4 helix are shown in solid and transparent blue ribbon representation, respectively. The alpha and beta carbon atoms of these extracellular side residues are highlighted in ball-and-stick representation. (*Inset*) An illustration of a potential Cd^{2+} bridge between a cysteine on S4 and a nonester phosphate oxygen atom from the outer leaflet.

on S4 and thus decrease the net charge as in A154C. In addition, the S3–S4 loop was found to be very flexible in our MD trajectories, and hence the Cd^{2+} bridge between Y200C and the S3–S4 loop could restrict the rearrangement of the loop, and in turn the movement of S4 (*SI Appendix*, Fig. S4 *D* and *E*).

To identify the factors underlying the Cd^{2+}-induced net charge reduction of the single cysteine mutants on the extracellular side of S4 (D213 to R223), we made additional mutants especially of the two negative residues D136 and D151, as they may form endogenous Cd^{2+} bridges with the cysteines. For L218C and V219C, the D136A mutation decreased the Cd^{2+} effect, but not for D151A. For V220C, both mutations showed negligible effect, while for L221C and A222C either D136A or D151A could rescue the Cd^{2+} effect, making the results inconclusive (Fig. 2*C*). To further test whether the single mutants would make Cd^{2+} bridges with the aspartates, we mutated them to a cysteine. For V219C and A222C, an additional cysteine mutation at position 136 or 151 both decreased the Cd^{2+} effect in contrast to the results of the single-cysteine mutants, eliminating the possibility of formation of a Cys–Cd^{2+}–Cys bridge. In addition, a negative control mutation, L137S, can also relieve the Cd^{2+} effect.

No periodicity was detected in the reduction of the maximum net charge and the shift of the half-maximum activation voltage ($V_{1/2}$) (*SI Appendix*, Fig. S5*A*), pointing to factors other than the Cys–Cd^{2+}–Asp bridge that likely underlie the Cd^{2+} effect. We then evaluated the possibility that these effects were mediated by Cys–Cd^{2+}–lipid interactions. We increased the external Cd^{2+} concentration to 1 mM and found a notable decrease of the net charge for A222C/D136A and A222C/D151A but not for L225C/D136A and L225C/D151A which were used as a control, considering the concentration-dependent Cd^{2+} effect on the single mutants (*SI Appendix*, Fig. S5 *B–E*). Using V219 as an example, analysis of the MD trajectories suggested that the residues on the extracellular side of S4 are not in a favorable distance to form Cd^{2+} bridges with D136 and D151. However, they are positioned to make favorable contacts with the outer leaflet of lipids during S4 movement. Interestingly, this putative contact stopped right at R223 at the "up-plus" state (*SI Appendix*, Fig. S5 *F* and *G*). The agreement between the experimental and computational results suggests that specific single-cysteine mutants can form Cd^{2+} bridges with the phosphate oxygen atoms of membrane

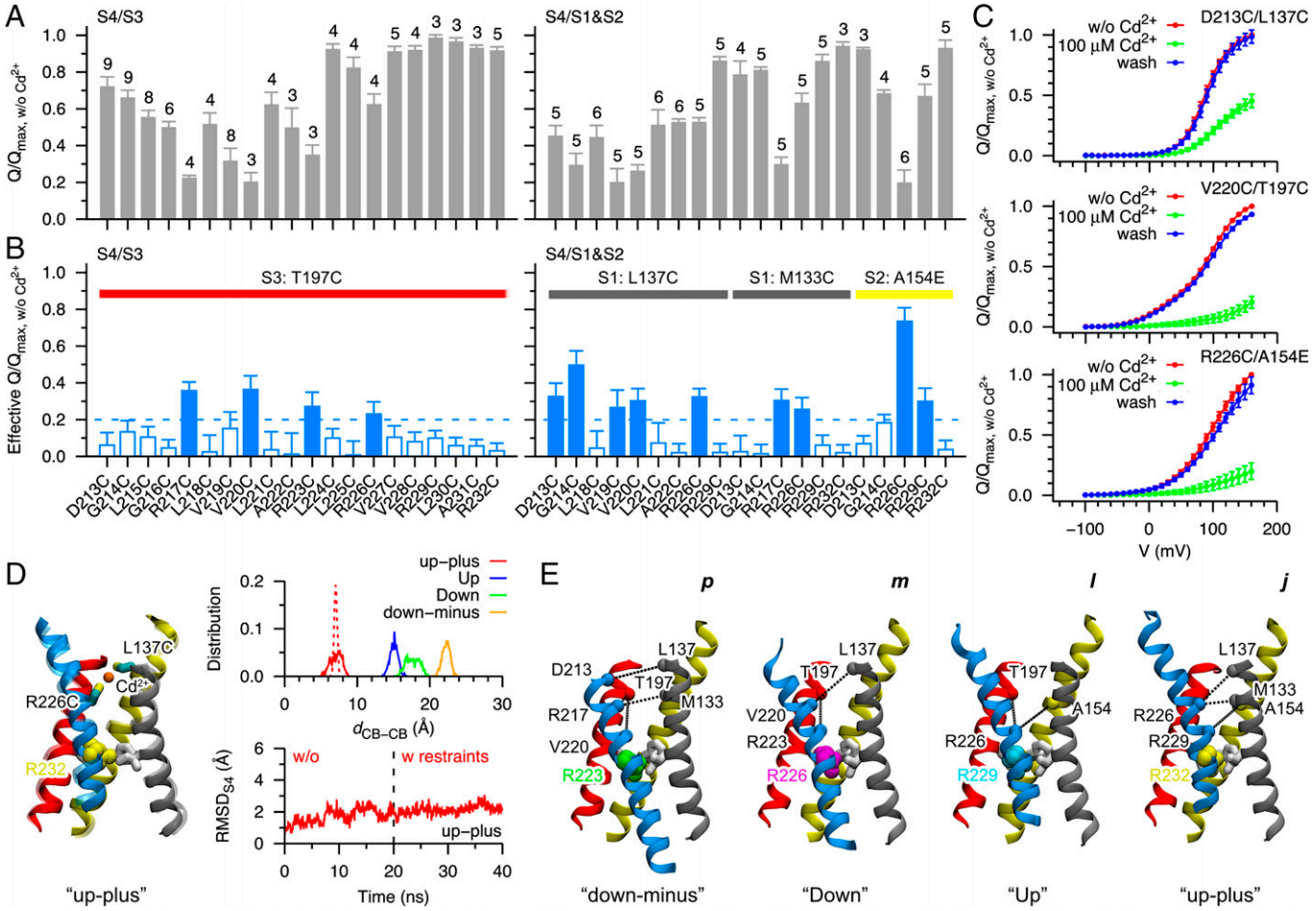

Fig. 3. State-dependent Cd^{2+} bridges formed by residues on the S4 and S1 to S3 helices. (*A*) The relative immobilization of OFF gating charge movement of double mutants of Ci-VSP at the maximum voltage in response to 100 μM Cd^{2+}. Error bars denote SD with the number of experiments being listed on the top of each bar. For mutants including R223C, the current amplitude at the end of the voltage pulse was used for the normalization and comparison. (*B*) The effective reduction of the normalized maximum net charge of the double mutants in *A* by considering the Cd^{2+} effect on each single mutant. A threshold of 0.2 (dashed line) was used to highlight the most likely interacting pairs (solid bar). Error bars denote SD. (*C*) Representative normalized *Q-V* curves of double mutants in the absence (red), in the presence (green), and after washout (blue) of 100 μM Cd^{2+}. Error bars denote SD with the same sample sizes as in *A*. (*D*, *Left*) Comparison of the conformation of the "up-plus" state Ci-VSD before (transparent) and after (solid) a restrained MD simulation with the R226C-Cd^{2+}-L137C bridge. (*D*, *Right*) Distance distributions (n = 1,000) of the beta carbon atoms of R226C and L137C in the MD simulations of the double mutant Ci-VSD (R226C/L137C) in different states (solid line) and in the restrained MD simulation of the double mutant Ci-VSD in the "up-plus" state only (dashed line) (*Top*) and the RMSD of the backbone atoms of S4 in the MD and restrained MD simulations of the "up-plus" state Ci-VSD mutant (*Bottom*). During the restrained MD simulation, the geometry of the Cys–Cd^{2+}–Cys bridge was harmonically restrained. (*E*) Projection of the state dependent Cd^{2+} bridge interactions suggested by restrained MD simulations into the four conformational states of Ci-VSD: "down-minus" (D213C/L137C, R217C/M133C, R217C/T197C, and V220C/T197C), "Down" (R223C/T197C and V220C/L137C), "Up" (R226C/T197C and R226C/A154E), and "up-plus" (R226C/L137C, R226C/M133C, and R229C/A154E). The alpha carbon atoms of interacting residues are shown in spheres and connected with dashed lines. The hydrophobic gasket-forming residues and the arginine residue in the middle of the gasket are shown in sticks and vdW representation, respectively.

phospholipids, a result that is fully consistent with the "up-plus" state as the outermost state of Ci-VSD (Fig. 2*D*).

Based on results from the single Cys mutants, we evaluated the Cd^{2+} effect on double mutants to investigate the residue–residue interactions that might define further structural constraints between S4 and S1 to S3. The T197C on S3 was first examined against the cysteine mutants on S4 (Fig. 3*A*). By considering the effect of single mutants, we found four notable bridging sites with a periodicity of three residues overlapping with the positions R217C, V220C, R223C, and R226C (Fig. 3*B*). To fully explore this conformational space, we also examined the partner mutants on S1 (M133C and L137C) and S2 (A154E) and found nine additional bridges (Fig. 3 *A* and *B*). As in the single-Cys mutant experiments, the reduced gating currents of double mutants could be restored after the washout (Fig. 3*C*). Restrained MD simulations of the double mutants forming Cd^{2+} bridges were then carried out to verify the most likely state(s) at which each bridge forms (Fig. 3*D* and *SI Appendix*, Fig. S6 *A–D*). In short, we built models for each double mutant at all the four states: "down-minus," "Down," "Up," and "up-plus." By analyzing the distance distribution of the beta carbon atoms of the two mutated residues, we were able to evaluate the bridge-forming state. An explicit Cd^{2+} bridge was then introduced into the specific model by inserting a Cd^{2+} ion and protonating the cysteine residue(s) (45). We note that because of the lack of accurate force fields for the metal bridge, external bond and angle restraints needed to be imposed to maintain the Cd^{2+} bridge (41). However, slight movements of S4 can always achieve an appropriate bridge while avoiding the breakdown of its secondary structure as shown by the backbone root-mean-square deviation (RMSD) of S4. These bridges can be perfectly projected onto their respective structures (Fig. 3*E*). Together with information from the unpaired double mutants, we conclude that other than the four major states evaluated here it is unlikely that the S4 segment is able to populate additional conformational states under physiological conditions. For instance, R217C can form a bridge with T197C in the

"down-minus" state, but the one helix turn above residue G214C is clearly unable to form stable interactions with T197C. Also, D213C and G214C can form bridges with L137C in the "down-minus" state but are unable to form bridges with M133C, which is one helix turn below L137C. These results lead us to conclude that S4 cannot move further down from the "down-minus" state (itself a low-probability event). For the upward S4 movement, R229C/A154E and R226C/M133C can form bridges at the "up-plus" state, but R232C/A154E and R229C/M133C cannot form bridges, implying that the "up-plus" state is the terminal state in any activating upward gating movement of S4. Based on restrained MD simulations we also found that distance should not be the only criterion that determines successful Cd^{2+} bridge formation. The space between two cysteine residues may have been previously occupied by other bulky or charged residue(s) preventing Cd^{2+} binding, or side-chain rotamer variability could lead to unfavorable orientations while still in a bridging distance, inhibiting bridge formation without unfolding the helix (*SI Appendix*, Fig. S6 *E–H*). Therefore, interpretation and design of metal bridges in the absence of structural information must be done with a healthy dose of caution.

State-Dependent Proton Currents in Single Ci-VSD S4 Mutants. Single mutations of gating charge arginines on S4 have been found to cause ionic leak through the VSDs of voltage-gated ion channels (42–44, 46, 47), the so-called "omega current" or "gating pore current." Continuous inward currents were also observed in our recording of R223C at potentials more negative than −20 mV. As *N*-methyl-D-glucamine (NMDG) was the only cation in our external recording buffer, we suspected that the inward currents were carried by protons. To test whether protons can permeate through other single mutants, we recorded the gating currents again at different external pH values (pH_o). A clear effect was observed on the mutants of three gating charge arginines (R223C, R226C, and R232C), especially the two outermost gating residues, in agreement with the study of single-histidine substitution of these residues (42). Other S4 single-cysteine mutants had minimal effects on the net charge, although the kinetics were faster at high pH_o than at low pH_o (Fig. 4*A* and *SI Appendix*, Fig. S7 *A* and *B*). In the case of both R223C and R226C current magnitude increased at lower pH_o, yet each mutant showed distinct current characteristics (Fig. 4*B*). R223C facilitated a steady leaky proton current similar to the typical "omega current," while R226C exhibited a gating current like transient leaky proton current. This

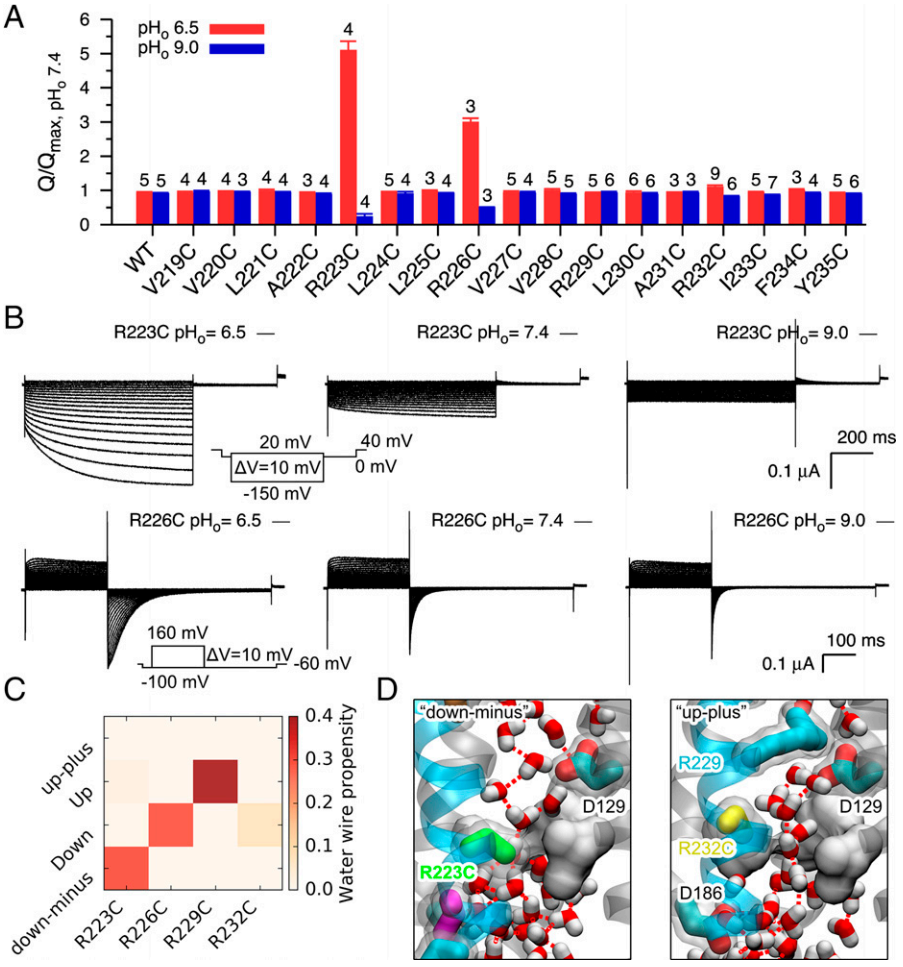

Fig. 4. State-dependent proton conduction through single cysteine mutants informs on the Ci-VSD conformations. (*A*) Changes of the maximum OFF net charge of WT and single cysteine mutants of Ci-VSP in response to the acidification of the external buffer. The net charge *Q* was normalized with respect to the maximum value at pH_o 7.4. The current amplitude of R223C at the end of the voltage pulse was used for the normalization and comparison. Error bars denote SD with the number of experiments being listed on the top of the bars. (*B*) Representative currents for R223C and R226C with the external recording buffer at different pH values. (*Insets*) Voltage pulse protocols used to elicit the currents. (*C*) Propensity of the formation of a continues hydrogen-bonded water wire connecting both sides of the mutated VSD at different states. Snapshots from the last 30-ns trajectory of each 50-ns MD simulation were used for the calculation (n = 3,000). (*D*) Snapshots of the R223C and R232C mutants at the "down-minus" and "up-plus" states, respectively. Instantaneous hydrogen bonds between water molecules inside the VSD are highlighted in dashed lines. The hydrophobic gasket is shown in surface representation for clarity.

suggests that proton leaks through R226C only at certain intermediate state(s) before the VSD finally reaches its terminal "down-minus" state, a state incompatible with R226C-carried omega currents.

To elucidate the mechanism of the state-dependent proton conduction, we carried out MD simulations of the single-cysteine mutants of the four gating residues at four major states and analyzed continuous water wire propensity in the aqueous crevices of the VSDs (Fig. 4 *C* and *D*). It has been suggested that proton conduction can be achieved if there is a continuous water wire connecting the extracellular and intracellular solutions (48, 49). R223C and R226C have a high water wire propensity at the "down-minus" and "Down" states, respectively. It is in good accord with our functional and computational data: The R223C mutant populates the "down-minus" state at negative potentials, resulting in steady inward proton currents as in the recordings. However, based on water wire analysis, the R226C mutant cannot conduct proton currents at the final "down-minus" state as in the R223C mutant but can conduct in the intermediate "Down" state. This explains why only transient inward proton currents were observed in the R226C mutant mixed with the OFF gating currents, both of which will be ceased when the VSD reaches the ending "down-minus" state.

For R232C, water molecules are able to hydrate the central hydrophobic gasket region in the "up-plus" state. However, the water wire was blocked by the salt bridge formed between R229 and D129, preventing the connection between the extracellular and intracellular solution and the steady outward proton permeation under depolarization. R229C also had a high water wire propensity at the "Up" state, but its pH dependence observed experimentally was marginal. Given its large negative $V_{1/2}$ shift (-51.70 ± 0.73 mV compared with 53.73 ± 0.46 mV of WT) and its faster kinetics compared with R226C, it is possible that this mutant exhibits very short "Up" state dwell times (*SI Appendix*, Figs. S5*A* and S7 *A* and *B*). In addition, the maximum net OFF charge of R229C is much smaller than others, the effect of noise and protein run-down may also weaken the pH effect (*SI Appendix*, Fig. S7*C*). These results further suggested that the "down-minus" state is the end state of the downward movement, and the occupancy of one gating residue at the hydrophobic gasket site and the salt bridges between the gating residues and D129 are critical for preventing omega currents through the WT VSD (*SI Appendix*, Fig. S7*D*).

Discussion

In this study, we investigated the gating mechanism of Ci-VSP using MD simulations and electrophysiological experiments to evaluate the influence of transmembrane voltage on the VSD energy landscape. We find that the gating cycle of Ci-VSD comprises four major states, where one of the four gating charge residues occupies the center hydrophobic gasket at each state at a time. In response to voltage changes, the S4 segment undergoes a set of sequential stepwise movements: one helix turn or one "click" transition associated with the translocation of roughly one gating charge at each step, yielding a total gating charge of $\sim 3\ e_0$ for the complete cycle.

It is important to acknowledge that there are limitations of our current structural models and MD simulations. First, we only built and simulated the Ci-VSD-alone model, due to the lack of a full-length structure of Ci-VSP or any VSPs. The cytosolic enzyme domain, connected to the VSD through a 16-residue-long linker, may influence the free energy landscape of Ci-VSD, e.g., by further stabilizing the "down-minus" state in negative potentials. Second, based on structural alignment of the crystal structures of the "Up" and "Down" states Ci-VSD and the proposed "click" model, we used two reaction coordinates to describe the translocation and rotation of the S4 segment along and around its axial axis, respectively. However, the S4 segment is not a straight and rigid helix; bending of S4 during rotation, tilting of S4 during translocation, and folding/unfolding of residues at the two ends of S4 upon gating are additional (hidden) degrees of freedom that are not explicitly handled by the two reaction coordinates used in the current study. To limit the influence of the hidden degrees of freedom, C_α atoms of the residues in the middle part of S4 having insignificant bending and tilting motions were used to define the reaction coordinates.

Engineering a Cd^{2+} bridge is a widely used approach to study residue–residue interactions in VSDs. Such bridges are Cd^{2+}-concentration-dependent, low-strength, and reversible and have a high spatial resolution (17, 21). Our electrophysiological data show that external Cd^{2+} can influence the gating currents of single-cysteine mutants on the S1 to S3 segments (A154C, Y200C) and the extracellular side of S4 (D213C–R223C), but not for others (M133C, L137C, T197C on S1 to S3 and L224C–R232C on the intracellular side of S4), which complicates the design and interpretation of Cd^{2+} bridges formed between double mutants. Further computational and electrophysiological results suggest that Cd^{2+} bridges between Y200C and negatively charged residues on the S3–S4 loop, Cd^{2+} trapped in the extracellular water crevice by A154C or Y220C, and Cd^{2+} bridges between the single mutants (D213C–R223C) and lipid headgroups are underlying the Cd^{2+} effect of these single mutants. To decipher the state(s) at which each Cd^{2+} bridge is formed is challenging. Using restrained MD simulations with an explicit Cd^{2+} bridge, we are able to pin down the corresponding states for the 11 pairs of notable interactions and show that S4 cannot move further upward than the "up-plus" state or further downward than the "down-minus" state.

Given recent breakthroughs in cryo-EM, a number of VSD structures in two different states have now been determined. These enable us to inspect the movement of other VSDs in an alternative way using the experience gained from the study of Ci-VSD. The S4 segment of the VSDs with available structures has three major secondary structure conformations: α-helical (20), 3_{10}-helical (34), and a combination of α-helical and 3_{10}-helical (37). This pattern is maintained throughout different states of the same VSD, although S4 is not always a single continuous helix; e.g., in the HCN channel (37, 50) the S4 segment breaks into two helices in the hyperpolarization state (*SI Appendix*, Fig. S8). Superimposition of the two structures of the same VSDs shows that the conformation of the S1 to S3 segments is quite stable, and the overall position of gating residues and the region of the α-helix/3_{10}-helix along S4 in relative to S1 to S3 remain approximately the same, as shown in the MD simulation study of the Shaker K^+ channel VSD (17). It implies that one gating residue will occupy its adjacent gating residue's position in a one-step movement of S4, just as what was observed experimentally in Ci-VSD. For the S4 segment having both α-helical and 3_{10}-helical regions, a continuous α-helical to 3_{10}-helical or 3_{10}-helical to α-helical transition will take place for residues in the boundary of the two helical conformations, while interrupting the secondary structural transition will impede the S4 movement and channel activation (51). Therefore, to fulfill this type of movement, the α-helical S4 segment will translate along and rotate around its axis (the conventional helical screw motion), the 3_{10}-helical S4 segment will translate along its axis without any rotation (the conventional helical sliding motion), and the α-helical/3_{10}-helical S4 segment will

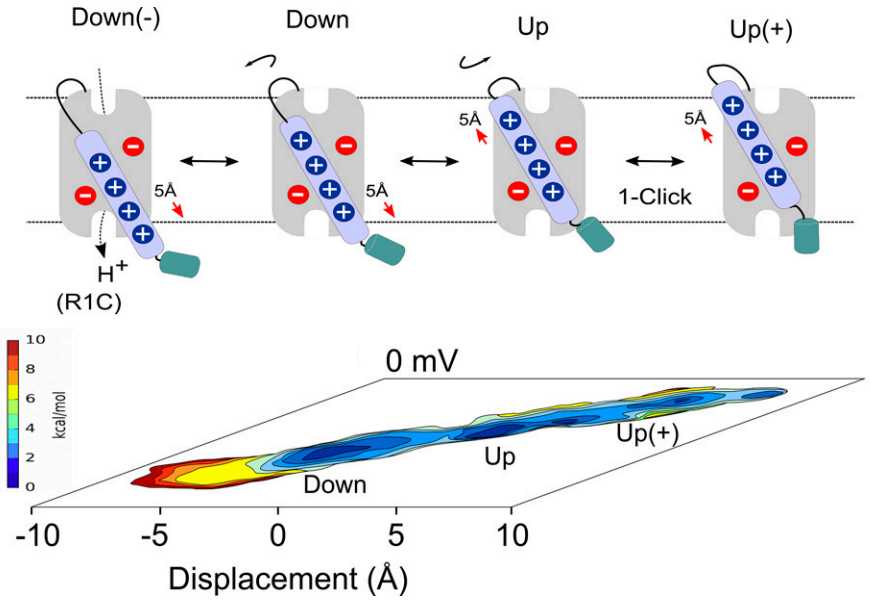

Fig. 5. Voltage sensor gating mechanism as a series of quantized "clicks." The energy landscape of a prototypical VSD (shown as a two-dimensional PMF at 0 mV) defines major conformational states along the S4 movement gating cycle. In Ci-VSD, four putative conformational states, Down, Up, down-minus [Down(−)], and up-plus [Up(+)] are related by sequential translations (of around 5 Å) and rotations to and from each adjacent state. Transmembrane voltage biases the energy landscape, triggering these transitions. Mutating the first gating charge to cysteine (R1C) leads to a proton-conductive sensor under hyperpolarizing potentials [i.e., populating the Down(−)].

undergo both translocation and rotation at the α-helix region and translocation alone at the 3_{10}-helix region (a combination of helical screw and sliding motion).

Thus, the "click" model (Fig. 5) could be a simplified and generalized model for the movement of all the VSDs, compared with the conventional "helical screw" and "helical sliding" models, so that one helix turn or one "click" represents the basic element of the movement of S4 and corresponds to a complete transition between two adjacent major states. Our working hypothesis is that, for hydrophobic-plug-containing sensors, S4 movement is "quantized" in the sense that S4 can only move in clicks defined by the relative position of existing countercharges. These vary according to the VSD type, explaining the wide range of voltage dependences among voltage sensors (34–37). These clicks would be defined by either simple major S4 axis translations, rotations, or secondary structure (alpha or 3_{10}) helical transitions. There are, however two important caveats. First, this picture does not consider that the field might be so sharply focused that each click could effectively move more than one charge equivalent; second, it assumes that the field is constantly focused during gating. These two parameters remain largely unknown. The present results should lead to further evaluation of unsolved functional states in other VSDs by designing specific mutations and introducing state-dependent metal bridges or disulfide bonds and to investigating detailed mechanisms and potential treatment of channelopathies caused by missense mutations in VSDs.

Materials and Methods

Four all-atom simulation systems were built using the crystal structures of Ci-VSD in the "Up" (Protein Data Bank [PDB] ID code: 4G7V) and "Down" (PDB ID code: 4G80) states (20) and the homology models of Ci-VSD in the "up-plus" and "down-minus" states. The protein was embedded into a lipid bilayer solvated in 0.1 M NaCl solution using the program VMD (52). MD simulations were performed using the program NAMD (53). The centroid structures of the four equilibrated systems were used to generate other simulation systems with in silico mutations and for restrained molecular dynamics simulations with an explicit Cd^{2+} bridge (40, 41). Targeted MD simulations, string method with swarms of trajectories, self-learning adaptive umbrella sampling were used to generate starting configurations for H-REMD umbrella sampling at different membrane potentials. Two reaction coordinates, *distanceZ* and *spinAngle*, defined using the collective variables interface (Colvars) module (54), were used in the free energy calculations to describe the translocation and rotation of S4, respectively. The structural coordinates of the four protein centroids are available in ModelArchive (https://www.modelarchive.org/) with the accession codes ma-w3dlu ("down-minus"), ma-2z0i0 ("Down"), ma-3visi ("Up"), and ma-ehsti ("up-plus").

Gating currents were recorded on a cut-open oocyte voltage-clamp setup (55, 56) using in-house software GPatch. The complementary DNA of the catalytically inactive mutant of Ci-VSP (C363S) (4), referred to as the WT Ci-VSP, was cloned into the pSP64T vector and used as background for all the mutations. Complementary RNA was transcribed in vitro using the linearized plasmids containing WT or mutant Ci-VSP with the mMessage mMachine SP6 transcription kit (Ambion; Invitrogen). *SI Appendix, Materials and Methods* includes more detailed methods for MD simulations, molecular biology, and electrophysiological recordings.

Data, Materials, and Software Availability. All study data are included in the article and/or *SI Appendix*.

ACKNOWLEDGMENTS. We thank the Francisco Bezanilla laboratory at the University of Chicago for providing oocytes and extended discussions on Ci-VSP cut-open oocyte experiments; Dr. David Medovoy for starting the free energy calculations; Dr. Giacomo Fiorin and Dr. Jérôme Hénin for advice on the usage of the Colvars module; Drs. Qufei Li, Tian Li, Michael David Clark, Carlos A. Z. Bassetto, Jr., Francisco Bezanilla, and the members of the E.P. and B.R. laboratories for helpful advice and discussions. R.S. specially thanks Dr. João Carvalho-de-Souza for cut-open voltage clamp training and Ms. Wieslawa Milewski for molecular biology training. This work was supported by NIH grants GM057846 (E.P.) and GM062342 (B.R.). Computer resources came from an allocation on the Beagle supercomputer at the University of Chicago and an allocation on the Blue Waters supercomputer at the National Center for Supercomputing Applications at the University of Illinois at Urbana–Champaign.

1. F. Bezanilla, How membrane proteins sense voltage. *Nat. Rev. Mol. Cell Biol.* **9**, 323–332 (2008).
2. W. A. Catterall, Ion channel voltage sensors: Structure, function, and pathophysiology. *Neuron* **67**, 915–928 (2010).
3. F. Windler *et al.*, The solute carrier SLC9C1 is a Na^+/H^+-exchanger gated by an S4-type voltage-sensor and cyclic-nucleotide binding. *Nat. Commun.* **9**, 2809 (2018).
4. Y. Murata, H. Iwasaki, M. Sasaki, K. Inaba, Y. Okamura, Phosphoinositide phosphatase activity coupled to an intrinsic voltage sensor. *Nature* **435**, 1239–1243 (2005).

5. F. Bezanilla, Gating currents. *J. Gen. Physiol.* **150**, 911–932 (2018).
6. C. A. Ahern, J. Payandeh, F. Bosmans, B. Chanda, The hitchhiker's guide to the voltage-gated sodium channel galaxy. *J. Gen. Physiol.* **147**, 1–24 (2016).
7. S. Noreng, T. Li, J. Payandeh, Structural pharmacology of voltage-gated sodium channels. *J. Mol. Biol.* **433**, 166967 (2021).
8. Y. Okamura, A. Kawanabe, T. Kawai, Voltage-sensing phosphatases: Biophysics, physiology, and molecular engineering. *Physiol. Rev.* **98**, 2097–2131 (2018).
9. S. Sakata, Y. Okamura, Phosphatase activity of the voltage-sensing phosphatase, VSP, shows graded dependence on the extent of activation of the voltage sensor. *J. Physiol.* **592**, 899–914 (2014).
10. J. Wu *et al.*, Structure of the voltage-gated calcium channel Ca(v)1.1 at 3.6 Å resolution. *Nature* **537**, 191–196 (2016).
11. J. Sun, R. MacKinnon, Cryo-EM structure of a KCNQ1/CaM complex reveals insights into congenital long QT syndrome. *Cell* **169**, 1042–1050.e9 (2017).
12. X. Pan *et al.*, Structure of the human voltage-gated sodium channel $Na_v1.4$ in complex with β1. *Science* **362**, eaau2486 (2018).
13. M. D. Clark, G. F. Contreras, R. Shen, E. Perozo, Electromechanical coupling in the hyperpolarization-activated K^+ channel KAT1. *Nature* **583**, 145–149 (2020).
14. T. Li *et al.*, Structural basis for the modulation of human KCNQ4 by small-molecule drugs. *Mol. Cell* **81**, 25–37.e4 (2021).
15. E. Palovcak, L. Delemotte, M. L. Klein, V. Carnevale, Evolutionary imprint of activation: The design principles of VSDs. *J. Gen. Physiol.* **143**, 145–156 (2014).
16. L. Delemotte, M. A. Kasimova, M. L. Klein, M. Tarek, V. Carnevale, Free-energy landscape of ion-channel voltage-sensor-domain activation. *Proc. Natl. Acad. Sci. U.S.A.* **112**, 124–129 (2015).
17. U. Henrion *et al.*, Tracking a complete voltage-sensor cycle with metal-ion bridges. *Proc. Natl. Acad. Sci. U.S.A.* **109**, 8552–8557 (2012).
18. V. Yarov-Yarovoy *et al.*, Structural basis for gating charge movement in the voltage sensor of a sodium channel. *Proc. Natl. Acad. Sci. U.S.A.* **109**, E93–E102 (2012).
19. J. R. Groome, L. Bayless-Edwards, Roles for countercharge in the voltage sensor domain of ion channels. *Front. Pharmacol.* **11**, 160 (2020).
20. Q. Li *et al.*, Structural mechanism of voltage-dependent gating in an isolated voltage-sensing domain. *Nat. Struct. Mol. Biol.* **21**, 244–252 (2014).
21. F. V. Campos, B. Chanda, B. Roux, F. Bezanilla, Two atomic constraints unambiguously position the S4 segment relative to S1 and S2 segments in the closed state of Shaker K channel. *Proc. Natl. Acad. Sci. U.S.A.* **104**, 7904–7909 (2007).
22. W. A. Catterall, Structure and function of voltage-gated sodium channels at atomic resolution. *Exp. Physiol.* **99**, 35–51 (2014).
23. X. Tao, A. Lee, W. Limapichat, D. A. Dougherty, R. MacKinnon, A gating charge transfer center in voltage sensors. *Science* **328**, 67–73 (2010).
24. J. A. Freites, E. V. Schow, S. H. White, D. J. Tobias, Microscopic origin of gating current fluctuations in a potassium channel voltage sensor. *Biophys. J.* **102**, L44–L46 (2012).
25. F. Khalili-Araghi *et al.*, Calculation of the gating charge for the Kv1.2 voltage-activated potassium channel. *Biophys. J.* **98**, 2189–2198 (2010).
26. C. A. Villalba-Galea, Corrigendum: Voltage-controlled enzymes: The new Janus Bifrons. *Front. Pharmacol.* **6**, 109 (2015).
27. H. Iwasaki *et al.*, A voltage-sensing phosphatase, Ci-VSP, which shares sequence identity with PTEN, dephosphorylates phosphatidylinositol 4,5-bisphosphate. *Proc. Natl. Acad. Sci. U.S.A.* **105**, 7970–7975 (2008).
28. T. Kurokawa *et al.*, 3′ Phosphatase activity toward phosphatidylinositol 3,4-bisphosphate [PI(3,4)P2] by voltage-sensing phosphatase (VSP). *Proc. Natl. Acad. Sci. U.S.A.* **109**, 10089–10094 (2012).
29. D. Keum, M. Kruse, D.-I. Kim, B. Hille, B.-C. Suh, Phosphoinositide 5- and 3-phosphatase activities of a voltage-sensing phosphatase in living cells show identical voltage dependence. *Proc. Natl. Acad. Sci. U.S.A.* **113**, E3686–E3695 (2016).
30. L. Liu *et al.*, A glutamate switch controls voltage-sensitive phosphatase function. *Nat. Struct. Mol. Biol.* **19**, 633–641 (2012).
31. S. S. Grimm, E. Y. Isacoff, Allosteric substrate switching in a voltage-sensing lipid phosphatase. *Nat. Chem. Biol.* **12**, 261–267 (2016).
32. S. C. Kohout, M. H. Ulbrich, S. C. Bell, E. Y. Isacoff, Subunit organization and functional transitions in Ci-VSP. *Nat. Struct. Mol. Biol.* **15**, 106–108 (2008).
33. M. Kruse, S. C. Kohout, B. Hille, Reinterpretation of the substrate specificity of the voltage-sensing phosphatase during dimerization. *J. Gen. Physiol.* **151**, 258–263 (2019).
34. G. Wisedchaisri *et al.*, Resting-state structure and gating mechanism of a voltage-gated sodium channel. *Cell* **178**, 993–1003.e12 (2019).
35. H. Xu *et al.*, Structural basis of Nav1.7 inhibition by a Gating-modifier spider toxin. *Cell* **176**, 702–715.e14 (2019).
36. T. Clairfeuille *et al.*, Structural basis of α-scorpion toxin action on Na_v channels. *Science* **363**, eaav8573 (2019).
37. C.-H. Lee, R. MacKinnon, Voltage sensor movements during hyperpolarization in the HCN channel. *Cell* **179**, 1582–1589.e7 (2019).
38. W. A. Catterall, Molecular properties of voltage-sensitive sodium channels. *Annu. Rev. Biochem.* **55**, 953–985 (1986).
39. H. R. Guy, P. Seetharamulu, Molecular model of the action potential sodium channel. *Proc. Natl. Acad. Sci. U.S.A.* **83**, 508–512 (1986).
40. E. Vargas, F. Bezanilla, B. Roux, In search of a consensus model of the resting state of a voltage-sensing domain. *Neuron* **72**, 713–720 (2011).
41. R. Shen *et al.*, Structural refinement of proteins by restrained molecular dynamics simulations with non-interacting molecular fragments. *PLOS Comput. Biol.* **11**, e1004368 (2015).
42. C. A. Villalba-Galea, L. Frezza, W. Sandtner, F. Bezanilla, Sensing charges of the Ciona intestinalis voltage-sensing phosphatase. *J. Gen. Physiol.* **142**, 543–555 (2013).
43. D. M. Starace, F. Bezanilla, A proton pore in a potassium channel voltage sensor reveals a focused electric field. *Nature* **427**, 548–553 (2004).
44. F. Tombola, M. M. Pathak, P. Gorostiza, E. Y. Isacoff, The twisted ion-permeation pathway of a resting voltage-sensing domain. *Nature* **445**, 546–549 (2007).
45. Y. Mishina, E. M. Duguid, C. He, Direct reversal of DNA alkylation damage. *Chem. Rev.* **106**, 215–232 (2006).
46. S. Sokolov, T. Scheuer, W. A. Catterall, Gating pore current in an inherited ion channelopathy. *Nature* **446**, 76–78 (2007).
47. D. Jiang *et al.*, Structural basis for gating pore current in periodic paralysis. *Nature* **557**, 590–594 (2018).
48. W. Han, R. C. Cheng, M. C. Maduke, E. Tajkhorshid, Water access points and hydration pathways in CLC H^+/Cl^- transporters. *Proc. Natl. Acad. Sci. U.S.A.* **111**, 1819–1824 (2014).
49. S. C. van Keulen *et al.*, Does proton conduction in the voltage-gated H^+ channel hHv1 involve Grotthuss-like hopping via acidic residues? *J. Phys. Chem. B* **121**, 3340–3351 (2017).
50. M. A. Kasimova *et al.*, Helix breaking transition in the S4 of HCN channel is critical for hyperpolarization-dependent gating. *eLife* **8**, e53400 (2019).
51. C. A. Z. Bassetto, Jr, J. L. Carvalho-de-Souza, F. Bezanilla, Metal bridge in S4 segment supports helix transition in Shaker channel. *Biophys. J.* **118**, 922–933 (2020).
52. W. Humphrey, A. Dalke, K. Schulten, VMD: Visual molecular dynamics. *J. Mol. Graph.* **14**, 33–38, 27–28 (1996).
53. J. C. Phillips *et al.*, Scalable molecular dynamics with NAMD. *J. Comput. Chem.* **26**, 1781–1802 (2005).
54. G. Fiorin, M. L. Klein, J. Hénin, Using collective variables to drive molecular dynamics simulations. *Mol. Phys.* **111**, 3345–3362 (2013).
55. M. Taglialatela, L. Toro, E. Stefani, Novel voltage clamp to record small, fast currents from ion channels expressed in Xenopus oocytes. *Biophys. J.* **61**, 78–82 (1992).
56. E. Stefani, F. Bezanilla, Cut-open oocyte voltage-clamp technique. *Methods Enzymol.* **293**, 300–318 (1998).